RESEARCH ARTICLE

Role of physical structure on performance index of crossflow microchannel heat exchanger with regression analysis

Salma Jahan[1] and Rehena Nasrin[1*]

*Correspondence:
rehena@math.buet.ac.bd

[1] Department of Mathematics,
Bangladesh University
of Engineering and Technology,
Dhaka, Bangladesh

Abstract

Microchannel heat exchangers have become the preferred choice in contemporary technologies like electronics, refrigeration, and thermal management systems. Their popularity stems from their compact design and exceptional efficiency, which outperform traditional heat exchangers (HE). Despite ongoing efforts, the optimal microchannels for enhancing heat management, minimizing pressure drop, and boosting overall performance have yet to be identified. This study seeks to deepen our understanding of heat transmission and fluid dynamics within a cross-flow microchannel heat exchanger (CFMCHE). Utilizing numerical modeling, it examines how various physical aspects—such as channel geometry, spacing between channels, the number of channels, and the velocity at the inlet—affect key performance indicators like pressure drop, effectiveness, Nusselt number, and overall efficiency. To enhance the design, we analyze six unique shapes of crossflow microchannel heat exchangers: circular, hexagonal, trapezoidal, square, triangular, and rectangular. We employ the Galerkin-developed weighted residual finite element method to numerically address the governing three-dimensional conjugate partial differential coupled equations. The numerical results for each shape are presented, focusing on the surface temperature, pressure drop, and temperature contours. Additionally, calculations include the efficacy, the heat transfer rate in relation to pumping power, and the overall performance index. The findings reveal that while circular shapes achieve the highest heat transfer rates, they underperform compared to square-shaped CFMCHEs. This underperformance is largely due to the increased pressure drop in circular channels, which also exhibit a 1.03% greater reduction in effectiveness rate than their square-shaped counterparts. Consequently, square-shaped channels, boasting a performance index growth rate of 53.57%, emerge as the most effective design among the six shapes evaluated. Additionally, for the square-shaped CFMCHE, we include residual error plots and present a multiple-variable linear regression equation that boasts a correlation coefficient of 0.8026.

Keywords: Cross-flow, Microchannel, Effectiveness, Heat exchanger, Performance index

Introduction

Microchannel heat exchangers are crucial parts of heating, ventilation, and air conditioning (HVAC) systems, automobile cooling systems, and electronics cooling systems because of their higher heat transfer efficiency, smaller size, and more compact design than traditional heat exchanger designs. Its heat transfer efficiency depends on various factors, like surfaces that can transmit heat, the temperature difference between the fluids, fouling, pressure drop, and fluid flow rate. [1–9] studied the heat transfer rate of fin-tube and plate-fin heat exchangers. According to Khairul et al. [1], the CuO/water nanofluids' heat transfer coefficient rose from 18.50 to 27.20%. In comparison, the volume concentration of the nanoparticles increased from 0.50 to 1.50% compared to water. They examined only the effects of water and CuO/water nanofluids on heat transfer performance; other nanofluids were not considered. They should have conducted a comprehensive analysis of the pumping power. Yaïci et al. [2] computationally investigate the effect of inlet air flow maldistribution on the thermo-hydraulic performance of plate-fin-and-tube heat exchangers, and their results indicate that up to 50% improvement or deterioration in the Colburn j-factor is found compared to the baseline case of a heat exchanger with a uniform inlet air velocity profile. This work does not thoroughly investigate the most effective header and distributor configurations to reduce maldistribution. Ajeeb et al. [3] conducted an experimental investigation into the operation of a compact gasket plate heat exchanger (PHEX) and discovered an increase in pressure drop of 8% and a heat transfer enhancement as the concentration of the nanoparticles increased to a maximum value of 27% at 0.2 vol%. The experiments may not apply to other operational scenarios because they were conducted under specific heating settings, most notably high temperatures. The optimal side ratio for heat exchangers was 0.25 by Cao et al. [4], who investigated the effects of various hexagonal side ratios on heat transfer capacity and fluid flow characteristics. Reducing the size of heat transfer equipment is possible by using graphene-based nanoparticles, which enhance heat transfer [5]. Natesan and Karinka [5] critically reviewed the numerous uses of graphene in heat exchangers and electronic devices and improved heat transfer in heat exchangers, heat pipes, and electronic components. However, the simulation's employed nanofluid is excessively costly, and its environmental and human health impacts are unknown. A quantitative analysis of the effects of flow maldistribution through compact plate-fin heat exchangers (HE) with baffle plates and wavy fins was conducted by Ismail et al. [6]. A good agreement was found after comparing the numerical and analytical results of the wavy fin to those of a rectangular fin. A multi-objective topology was created by Ghasemi et al. [7] to improve sink geometries and reduce pressure loss and heat resistance at the same time. Compared to typical (circular) in-line and staggered fins, the optimized topologies showed better cooling capabilities at lower pressure loss costs, proving the superiority of topology over pure sizing optimization. Using mathematical modeling, Kalantari et al. [8] conducted an analytical correlation to assess the importance of geometrical, design, and operating characteristics for conjugate heat transmission via fin and tube HE by varying *Re* numbers from 3000 to 12,000. The findings revealed a novel association that leads to a conjugate heat transfer forecast that is more accurate than its conventional non-conjugate counterpart. Still, it does not reflect all flow conditions accurately. Raei et al. [9] used a drag-reducing agent (DRA) nanofluid within a fin-and-tube HE to lower pressure

drops and examine the heat transfer performance. They demonstrated that 0.2-weight nanofluid can produce 20% more heat transfer at the cost of a 5% increase in pressure drop (without the addition of DRA). They might look into the impacts of other variables, including temperature, drag reduction, and flow rates.

Better temperature changes are possible with a double-tube heat exchanger than with some other types because it uses two concentric tubes for improved heat transmission. The heat transfer performance of water nanofluids (GNP/water) and graphene nano-platelets (GNP) via a double-tube-type heat exchanger (DTHE) was investigated and compared by Lima et al. [10] using computational fluid dynamics (CFD) simulation and experimental methods. Their findings showed a 28% increase in temperature gain at 0.025 weight percent GNP, indicating superior thermal performance. These results agree with those obtained from CFD modeling and empirical correlation calculations. Khosravi et al. [11] proposed an innovative design to improve the performance of DTHE. They demonstrated that, compared to a smooth tube, the convective heat transfer coefficient for the cold fluid could be raised by up to 22% when employing nanofluids as working fluids. The study did not look at pressure decrease or the overall effectiveness of heat transfer; instead, it solely examined the cavern pressure evaluation curve. The sensitivity analysis of heat transfer and heat exchanger effectiveness was studied by Shirvan et al. [12] using the response surface (RSM) approach considering the nanoparticle volume fraction ($0.01 \leq \phi \leq 0.05$) and Reynolds number ($50 \leq Re \leq 250$) by using Al_2O_3 nanofluid and found that the mean Nu number increased 57.70% with Re number when the nanofluid entered the outer pipe where $Re = 50$ to 150 and $\phi = 0$. They ignored the other nanofluids' effect. Bashtani and Esfahani [13] numerically examine the capacity of a DTHE with a simple and corrugated tube, assuming three distinct wave amplitudes and considering the k-ω shear stress transport (SST) turbulence model. The findings demonstrated that, compared to the primary heat exchanger, the corrugated HE's average Nu number was around 1.75 times higher, and its effectiveness ratio was 1.73 at similar Reynolds numbers. They did not conduct experimental research; they just performed numerical simulations. Using the Kays-Crawford model, Nasrin et al. [14] studied turbulent flow in a shell and tube heat exchanger (HEX). Their results showed that using 3% concentrated water-multi-walled carbon nanotube (MWCNT) nanofluid, a higher heat transfer rate (12.24%) was achieved compared to that of water, consequently enhancing the efficiency of this heat exchanger. For a range of Re numbers between 100 and 1000, the significance of geometrical parameters on the properties of heat transmission and water flow in microchannels was numerically examined by Gunnasegaran et al. [15]. They discovered that the rectangular heat sink with the minor hydraulic diameter performs better regarding pressure drop and friction factor out of all the shapes. Zhu et al. [16] offered a comparative study to discuss how well these geometric configurations performed regarding the overall performance factor, friction coefficient, entropy production, and average Nusselt number. The microchannel that combines elliptical rib columns and water droplet cavities appeared to be the most effective in all scenarios, achieving an overall performance factor of up to 1.513 at $Re = 331.32$ with $\alpha = 0.3$ and $\xi = 0.5$. Starace et al. [17] numerically investigated the heat transfer mechanism in cylindrical micro-pin–fin heat exchangers. They provided a methodical examination of flow boiling in a micro-pin–fin evaporator, covering heat transfer, thin-film dynamics, and

bubbles. They found that increasing the mass flow rate causes bubbles to grow more slowly and leave the nucleation sites earlier, which reduces the two-phase heat transfer.

Apart from the heat exchangers previously mentioned, flow-configuration-based heat exchangers such as crossflow, counterflow, and parallel flow heat exchangers are also employed to enhance heat transfer efficiency. Using numerical analysis, Mohammed et al. [18] investigated the effects of various nanofluids on the heat transfer characteristics and fluid flow through a square-shaped parallel flow microchannel HE with varying Reynolds numbers. They discovered that nanofluids could enhance the HE's thermal performance with only a slight increase in pressure drop. Still, they should have considered channel configuration, ignoring many characteristics that could impact overall performance, such as the friction factor, pressure drop, and Colburn factor. The flow through a parallel-plate micro-heat exchanger was studied statistically by Al-Nimr et al. [19] to examine its thermal and hydrodynamic properties. Although they did not examine all the other relevant variables in real-world applications, their results indicate that the number of transfer units (NTU) increases as the heat capacity ratio increases at a low Knudsen number. The efficiency of a new heat exchanger has been tested experimentally and theoretically by Kragh et al. [20]. They presented and designed a revolutionary counter-flow HE for cold climates that can continually defrost itself at outside air temperatures below freezing. Still, their geometry is more significant than any other geometry. Anjaneya et al. [21] investigated and compared the effectiveness of different microchannel heat sinks based on hydraulic diameter, surface area, and number of channels. The absence of experimental validation in the study could potentially improve the dependability of the CFD outcomes. They only used rectangular channels.

Larger in surface area and more efficient in heat transfer, cross-flow heat exchangers are cheap, simple to install, and widely used in various industries, including portable cooling systems and aircraft heat exchange. In a research experiment, Kalantari et al. [22] looked into the impact of a $CuFe_2O_4$/water nanofluid on the enhancement of the rate of heat transmission in a cross-flow type HE under turbulent flow at varying volume percentages of $CuFe_2O_4$/nanoparticle ($0 \leq \phi \leq 0.9\%$ vol.). A maximum performance evaluation criterion (PEC) improvement of 44.46% was observed when using nanofluids with a volume percentage of 0.1%. They only focused on a single nanofluid. Masitah et al. [23] provided heat transfer and effectiveness analysis based on a cross-flow heat exchanger physical model. The investigation reveals that heat is transported through heat transfer plates at an increasing air velocity. Effectiveness, on the other hand, rises when air velocity falls. Li et al.'s study [24] looked at the effects of the corrugation pitch, inlet cross-angle, and inlet temperature difference on the performance of a W-alloy vertical cross-flow corrugated plate heat exchanger (VC-CPHE), which has certain advantages over other heat exchangers in space reactor applications. They discovered that while the heat transfer coefficient somewhat decreases with increasing heat exchanger inlet temperature differential, overall heat transfer improves. A cross-flow printed circuit HE is a reduced-order dynamic model presented by Furlong et al. [25]. It assesses steady-state and transient performance, lessening fluctuations in heat-integrated reactors and intensification processes. Important factors influencing the transient response of large heat exchangers are initial variations in outlet temperatures from ideal-case models below 3.8% of unit step magnitudes, average differences

below 0.75%, and limited fluid velocity. Their representation of the model's behavior under particular operating conditions was imprecise, and they only used half-circular shape geometry, ignoring other shapes. By adjusting the number of heat pipes, fins, and the inlet velocity variation at the heat exchanger's inlet as fundamental parameters for determining the thermophysical quantities of interest, Nogueira [26] theoretically analyzed the temperature efficiency of HE through a cross-flow finned heat pipe heat exchanger (FHPHE) to control the quality of the air conditioning in operating rooms. They discovered that the global heat transport rate varies from 0.5% to 35%. Ghorbani et al. [27] focused on developing a numerical model and aimed to analyze the Nusselt number in the air and oil channels that agree well with classical developing flow correlations. They provided accurate temperature distributions in both fluid channels that closely matched the results of the experiments. Liu et al. [28] found that when the thermodynamic characteristics were examined using counter-flow and cross-flow plate-fin heat exchangers (PFHE), the efficacy of constant wall temperature boundary conditions increased by 35.8% and the heat flux increased by 22.8%. The study does not investigate the effects of different fluids. The study focuses on the thermodynamic characteristics of counterflow and crossflow PFHEs and does not consider other types of heat exchangers. Mangrulkara et al. [29] reviewed the most recent advancements and how they might enhance heat exchangers' thermal performance. They provided some suggestions for improving the next-generation cross-flow heat exchanger. Specifically, they suggested that tube shapes, fins, and winglets increase the heat exchanger's effectiveness. Moosavi et al. [30] performed a numerical comparison of the thermo-fluid behavior of wall-bounded and free cross-flow heat exchangers at a *Re* number of 40,000 using the unsteady Reynolds-averaged Navier–Stokes (URANS) method. Local *Nu* number distributions in the angular and spanwise directions showed significant changes. Still, the area-averaged mean *Nu* from 2 and 3D models for free heat exchangers shows no significant difference compared to wall-bounded heat exchangers. They only used circular-shaped channels, ignoring other shapes. The experimental study of calcium sulfate crystallization fouling in cross-flow heat exchangers was conducted by Jradi1 et al. [31] using RSM. According to the results of their suggested model, anhydrite ($CaSO_4$) is the primary crystal form that fools those forms on HE walls. This suggests that crystallization fouling controls the fouling process, for which fluid temperatures significantly raise the fouling resistance on the surface. Toolthaison and Kasayapanand [32] carried out experimental research using a modified air angle of attack with a constant flow rate and air at ambient conditions with varying velocities (ranging from 2 m/s to 7 m/s) to improve heat transfer of a nonfinal cross-flow HE. According to their findings, the adjusted air angle of attack technique can raise the heat transfer coefficient overall, but there was also an increase in pressure drop. Caceres et al. [33] used a numerical model, validated against preliminary experimental data collected in their laboratory for chilled water flowing in a single phase, to predict the transient response of a refrigerant-based crossflow HE as part of a close-coupled hybrid cooling system (CCHCS) since the use of refrigerants enhances the thermal performance of these systems. Starting from the results of the numerical analysis at the micro-scale, Starace et al. [34] proposed a potent alternative design procedure for the cross-flow compact heat exchangers design to find a wall

temperature distribution throughout and to determine the mass flow rate distributions on both sides. They found that the multi-scale approach yields more accurate results than the full-scale method.

Alonso et al. [35] examined membrane-based heat exchangers that may encounter serious freezing issues to achieve zero-energy buildings in cold climates. Nevertheless, smells can still transfer from extracted air to supplied air due to the delicate nature of membrane-based heat exchangers and the need for careful optimization. Mortean et al. [36] examined a cross-flow heat exchanger's theoretical and numerical thermal and hydrodynamic behavior. In addition, the predicted pressure decrease has some limitations, and the analysis was limited to square channels, so the results might not apply directly to heat exchangers with other channel geometries. Mitra and Ghosh [37] created a three-dimensional crossflow heat exchanger model that can regulate both balanced and unbalanced flows. Their model only uses rectangular channels; it ignores other geometries, transient behavior, irregular flow distribution, and fouling factors in performance analysis. Zhong et al. [38] tested a plate-fin total heat exchanger's (PFTHE) enthalpy efficacy and sensibility. According to the findings, the PFTHE's enthalpy efficacy and sensitivity and efficacy are best at 7.8% and 17.4% airflow rates, respectively. Understanding the improved PFTHE's relative effectiveness is limited because the study did not compare its performance with other heat exchanger types. Kang and Tseng [39] created a theoretical model that forecasts a micro-cross-flow heat exchanger's fluidic and thermal properties. The analytical findings demonstrate that the average temperature of the cold and hot side flows strongly and equally influences the pressure drop and the heat transfer rate. It is challenging to comprehend some design factors and how they impact pressure drop and heat transmission rate due to the sources' lack of information about the heat exchanger's dimensions.

According to the literature above, extensive research has been conducted on channel shape's impact on counterflow microchannel heat exchangers. Still, research has yet to be done on cross-flow microchannel heat exchangers. In addition, more research needs to be done on reducing the pressure drop, even though little has been done to improve heat transfer. There has yet to be any comparative research on the heat transfer mechanisms of various shapes in terms of specifics like pressure drop minimization and heat transfer optimization. However, more than dealing with a limited number of shapes is required. Thus, scientists ought to continue focusing on this issue as well as the following topics:

- No study has been done on effectiveness analysis through cross-flow through differently shaped microchannel heat exchangers.
- No study has been done on overall performance analysis through different shaped channel heat exchangers.
- No thorough research has examined how channel shapes affect effectiveness analysis.
- The performance evaluation and effectiveness of various CHMCHE geometries have not been compared.
- No research on the impact of channel distance and geometry has been the subject of comparative research.

- No research has been done on pressure drop minimization.

Thus, in this study, we investigate the following:

- We investigate increased heat transfer and fluid flow using variously shaped cross-flow microchannel heat exchangers.
- We explore how various channel forms affect heat transfer optimization and pressure drop minimization through a cross-flow microchannel heat exchanger.
- We look at the effectiveness and overall performance of different-shaped cross-flow microchannel heat exchangers.

From this study, researchers will benefit and be motivated to use cross-flow microchannel heat exchangers with appropriate channel shapes to enhance performance in hydraulic and thermal phenomena.

Physical modeling

The CFMCHE schematic figure in a square-shaped channel is presented in Fig. 1, and a 2D schematic sketch of trapezoidal, hexagonal, circular, square, rectangular, and triangular forms is shown in Fig. 2. Although the microchannel heat exchanger consists of 20-unit cells for symmetry and reduces computational time and cost, only a single unit of CFMCHE is chosen for this study. The physical structural properties are illustrated in Table 1. Water is considered the base fluid, and stainless steel is the solid material of CFMCHE. Table 2 contains a summary of both of their thermophysical characteristics. We use pressure $P = 0 \, Pa$ a at the outlet, 333 K at the hot inlet, and 298 K at the cold inlet to simulate the model. The Reynolds number is taken into consideration when computing the inlet velocities.

Regarding a variety of Reynolds numbers from 2 to 20, inlet velocities, dependent on the number, vary from 0.024 m/s to 0.24 m/s.

Mathematical modeling

The CFMCHE controlling equations provided below are extracted from Refs. [41]. According to [41], the flow exhibits all these properties: laminar, single phase, forced convection, viscous incompressible, and steady state.
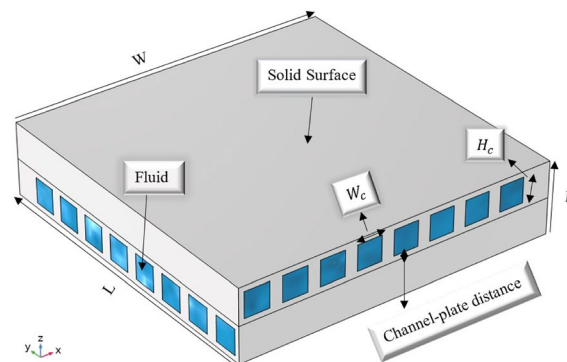

Fig. 1 Schematic diagram of the 3D computational domain of square-shaped CFMCHE
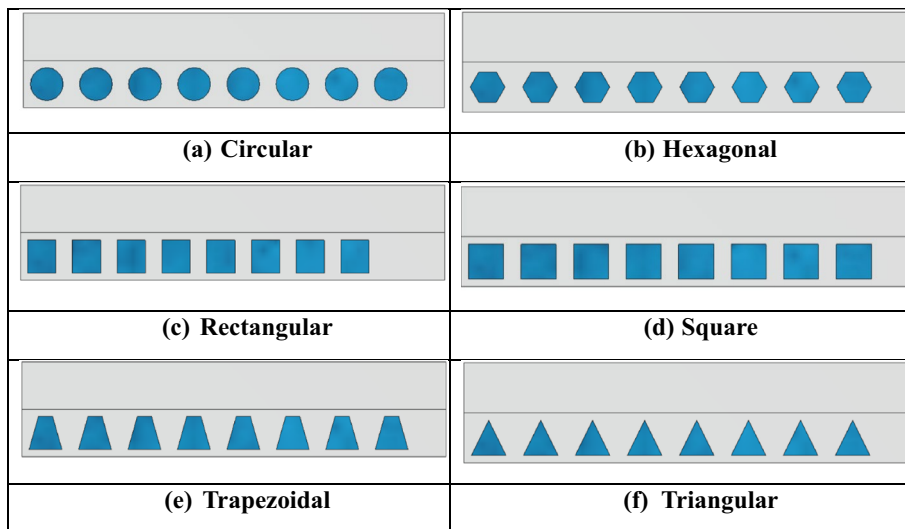
Fig. 2 **a–f** 2D computational domain for circular, hexagonal, rectangular, square, trapezoidal, and triangular-shaped CFMCHE

Table 1 Physical structural parameter of the CFMCHE

Physical parameters	L	H	W	L_{ch}	H_{ch}	W_{ch}	D_{or}	D_{ch}
Value (μm)	900	900	200	900	70	70	15	5

Table 2 Thermophysical characteristics of water [47] at $T = 298$K

Thermophysical properties	Stainless steel	Water
Density ρ[kg/m^3]	7800	997
Dynamic viscosity μ[Pa s]:		0.001
Heat capacity at constant pressure C_p[J/kg K]	420	4178
Thermal conductivity k[W/mK]	15	0.609

$$\frac{\partial u}{\partial x} + \frac{\partial v}{\partial y} + \frac{\partial w}{\partial z} = 0, \tag{1}$$

$$\frac{\partial u}{\partial x} + v\frac{\partial u}{\partial y} + w\frac{\partial u}{\partial z} = -\frac{\partial p}{\partial x} + \frac{\mu_f}{\rho_f}\left(\frac{\partial^2 u}{\partial x^2} + \frac{\partial^2 u}{\partial y^2} + \frac{\partial^2 u}{\partial z^2}\right), \tag{2}$$

$$u\frac{\partial v}{\partial x} + v\frac{\partial v}{\partial y} + w\frac{\partial v}{\partial z} = -\frac{\partial p}{\partial y} + \frac{\mu_f}{\rho_f}\left(\frac{\partial^2 v}{\partial x^2} + \frac{\partial^2 v}{\partial y^2} + \frac{\partial^2 v}{\partial z^2}\right), \tag{3}$$

$$u\frac{\partial w}{\partial x} + v\frac{\partial w}{\partial y} + w\frac{\partial w}{\partial z} = -\frac{\partial p}{\partial z} + \frac{\mu_f}{\rho_f}\left(\frac{\partial^2 w}{\partial x^2} + \frac{\partial^2 w}{\partial y^2} + \frac{\partial^2 w}{\partial z^2}\right), \tag{4}$$

$$u\frac{\partial T}{\partial x} + v\frac{\partial T}{\partial y} + w\frac{\partial T}{\partial z} = \left(\frac{\kappa}{\rho C_p}\right)_f \left(\frac{\partial^2 T_f}{\partial x^2} + \frac{\partial^2 T_f}{\partial y^2} + \frac{\partial^2 T_f}{\partial z^2}\right), \tag{5}$$

$$k_s\left(\frac{\partial^2 T_s}{\partial x^2} + \frac{\partial^2 T_s}{\partial y^2} + \frac{\partial^2 T_s}{\partial z^2}\right) = 0, \tag{6}$$

The following are the applying boundary conditions [40]:

At all bottom inlet: $u = u_{in}, v = 0, w = 0, T_c = 298$K.
At all top inlet: $u = 0, v = v_{in}, w = 0, T_h = 333$K
At all outlets: $P = 0$
At top and bottom surfaces: symmetry ($\mathbf{u.n} = 0$ and $-\mathbf{n.q} = 0$)
At external walls: insulation $\frac{\partial T}{\partial n} = 0$
At solid–fluid interface: $k_f\left(\frac{\partial T}{\partial n}\right)_f = k_s\left(\frac{\partial T}{\partial n}\right)_s, T_s = T_f, u = v = w = 0.$

where, $\mathbf{n}$, $\mathbf{u}$, $\mathbf{q}$ are the unit outward normal vector, velocity vector, and heat transfer vector.

The following includes the required definitions for the current model along with their related expressions:

- Reynolds number [42],

$$Re = \frac{\rho_f u_{in} D_h}{\mu_f}. \tag{7}$$

- Hydraulic Diameter [42],

$$D_h = \frac{2W_{ch}H_{ch}}{W_{ch}+H_{ch}}. \tag{8}$$

- Heat transfer coefficient [45],

$$h = \frac{q}{A(T_h - T_c)}. \tag{9}$$

- Nusselt number [45],

$$Nu = \frac{hD_h}{k_f}. \tag{10}$$

- Total pressure drop [42],

$$\Delta P = \Delta P_c + \Delta P_h = (P_{ci} - P_{co}) + (P_{hi} - P_{ho}). \tag{11}$$

- Total Pumping power [18],

$$P_{pu} = Q_h\Delta P_h + Q_c\Delta P_c, \tag{12}$$

- Volumetric flow rate [18],

$$Q = N_{ch}A_{ch}u_{in}, \tag{13}$$

- Effectiveness [42],

$$\varepsilon = \frac{q_{actual}}{q_{max}}, \tag{14}$$

- Heat exchanger performance (Thermal) [42],

$$\eta = \frac{\varepsilon}{\Delta P}. \tag{15}$$

- Heat exchanger performance (Hydraulic) [42],

$$\eta^* = \frac{q}{P_{pu}}. \tag{16}$$

where, N_{ch} is number of channel, $q_{max} = mC_p(T_{hi} - T_{ci})$, and $q_{actual} = (mC_p)_h(T_{hi} - T_{ho}) = (mC_p)_c(T_{ci} - T_{co})$, are the maximum and actual heat transfer, respectively.

Numerical procedure

Galerkin's weighted residual methods have been used to solve the Navier–Stokes above Eqs. (1–6) and related boundary conditions [43]. This method uses meshing, essential in complicated geometry, to divide the solution domain into smaller parts called finite elements. These elements comprise non-uniform 10-node tetrahedron elements in the domain and 6-node triangle elements in the boundary. Refs. [44, 46] comprehensively details Galerkin's weighted residual approaches. For this solution process, the convergence criteria are specified as $|\psi^{n+1} - \psi^n| \leq 10^{-4}$ where n is the number of iteration and ψ is the function of dependent variables.

Mesh and grid test

The mesh utilized in this investigation for CFMCHE, which has circular, square, rectangular, trapezoidal, hexagonal, and triangular shapes, is shown in Fig. 3a–f. The domain's solution has been partitioned into non-uniform finite element meshes. Elements in the border consist of 6-node triangles and 10-node tetrahedrons. Through a square-shaped microchannel heat exchanger, shown in Fig. 4, five different types of grids are executed at $Re = 4$, channel number 11, and Channel distance 5 μm. The total number of meshes consists of 69,181 (coarser), 158,131 (coarse), 401,997 (normal), 1,644,033 (fine), and 32,352,494 (finer), respectively.

The computational times are 87 s, 164 s, 317 s, 1223 s, and 3836 s, respectively, and the number of elements is 69,181, 158,131, 401,997, 1,644,033, and 3,252,494, respectively. 2363.1401 [W/m²*K], 2366.6112 [W/m²*K], 2370.6531 [W/m²*K], 2371.5822 [W/m²*K], and 2371.7614 [W/m²*K] are the corresponding heat transfer coefficient values. The computation time increases considerably, but the heat transfer coefficients after normal meshes increase so marginally that it has an insignificant effect.
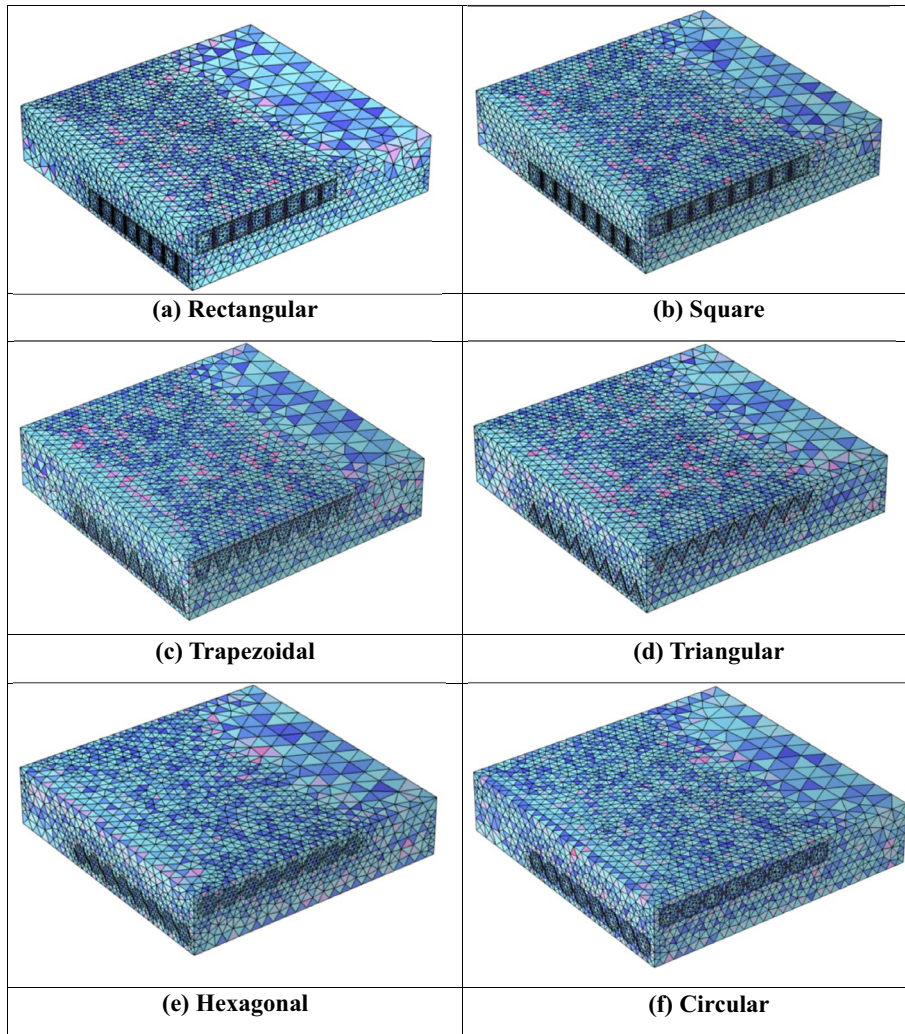
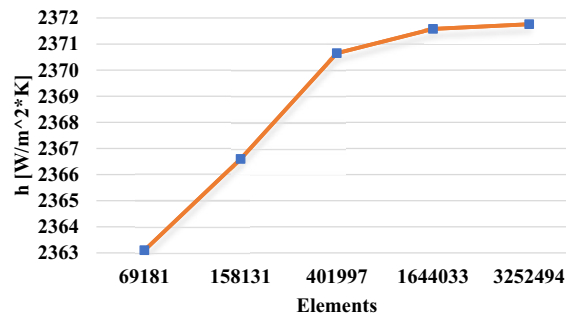**Fig. 3** A 3D mesh of the computational domain of different channel-shaped CFMCHE

Fig. 4 Grid test at $Re = 4$, channel number 11 and distance 5 μm

For the numerical simulation, we use a normal mesh for all shapes of heat exchange to balance computational cost and accuracy**.**

Results and discussions

Six different shapes with constant heat exchanger dimensions are used to investigate the overall performance of CFMCHE. In all cases, cold and hot fluids move at the same speeds ($u_{in} = v_{in}$). We compare our current model to Ahmed et al. [45] to verify its validity and discover a firm agreement. We can infer that our model is trustworthy based on the comparison findings. Our findings are categorized into three sections: the impact of Reynolds number, the effect of Channel distance, and the impact of channel number on *Nu* number, effectiveness, pressure drop, and overall performance index.
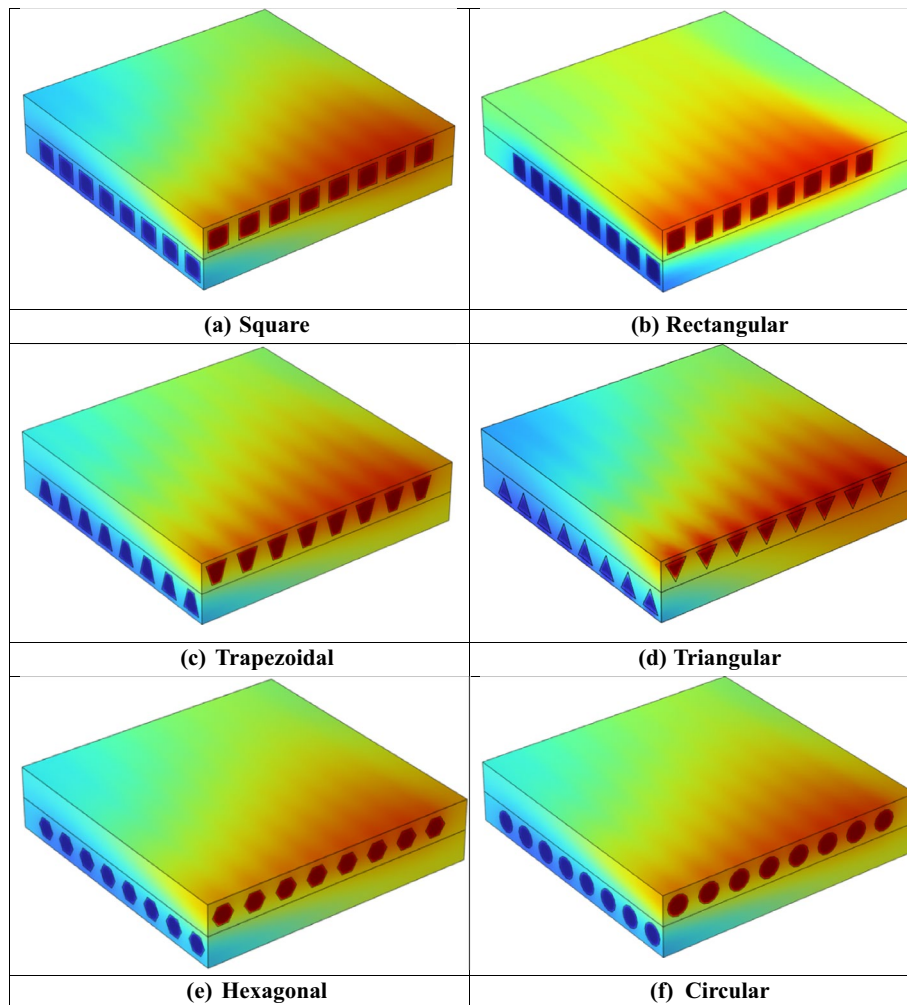

(a) Square **(b) Rectangular**

(c) Trapezoidal **(d) Triangular**

(e) Hexagonal **(f) Circular**

Fig. 5 Surface temperature of CFMCHE at channel number 8 and distance 35 μm

Role of channel shape

Surface temperature

Figure 5 shows the surface temperature profiles over six different-shaped microchannels, including square, rectangular, triangular, trapezoidal, circular, and hexagonal, by keeping the channel number fixed at 8, the distance between channels at 35 μm, and the Reynolds number at 20. The above statistics from Fig. 5 demonstrate that heat exchange occurs between cold and hot fluids, and temperature spreads across the surface. Out of these six designs, square and circular both have a greater hydraulic diameter (7×10^{-5} m), which means they should disperse more heat because the larger hydraulic diameter and increased surface area enable better heat transfer with faster temperature spreading. The square and trapezoidal shapes in this study disperse temperature more than other designs of similar size because of their extended surfaces at the edges. Extended surfaces promote better heat transfer and faster temperature spreading by allowing for a closer connection with the surrounding environment and more efficient heat transfer. This results in a larger surface area and greater temperature spreading. We notice that square shapes have a heat exchange rate of 0.43%, trapezoidal shapes have a rate of 0.41%, and triangular shapes have a rate of 0.36%. Among these six shapes, the temperature of the square shape spreads very well, in which hot and cold channels exchange more heat between them, and the temperature of the triangular shape applies less. After releasing heat through the heat exchanger wall, the fluid from the hot channel cools in the heat exchanger. Moreover, heat is transferred from the hot fluid to the cold channel, where the fluid gets heated.

Isothermal lines

Isothermal contour lines represent the region of constant temperature within the channel. These lines show how each channel's geometric variations impact the flow and heat
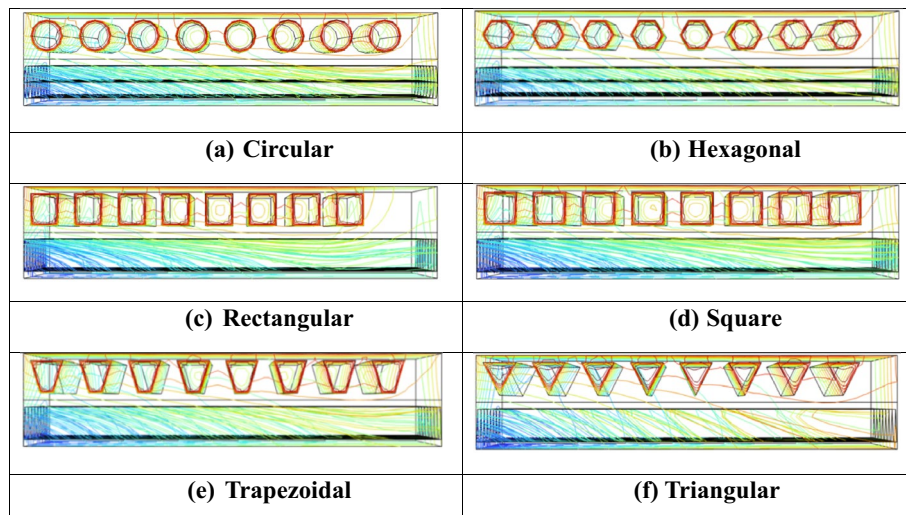

Fig. 6 Isothermal lines in the xz- plane for different CFMCHE with $Re = 20$

transfer properties. Because of its concentric isothermal contours, the circular channel facilitates consistent heat transfer across its cross-section. Hexagonal channels exhibit uneven isothermal contours and intricate flow patterns. The uneven aspect ratio of rectangular channels results in elongated isothermal contour lines. Uniform flow distributions and symmetric heat transfer are provided by square channels, which lead to clearly defined isothermal contour lines. Because of its sharp corner edge, the triangular channel displays non-uniform temperature distribution, asymmetric isothermal contour lines, and concentric heat transfer distribution along the channel wall. The trapezoidal channel displays both uniform and non-uniform flow distribution because it combines the features of the rectangular and triangular channels.
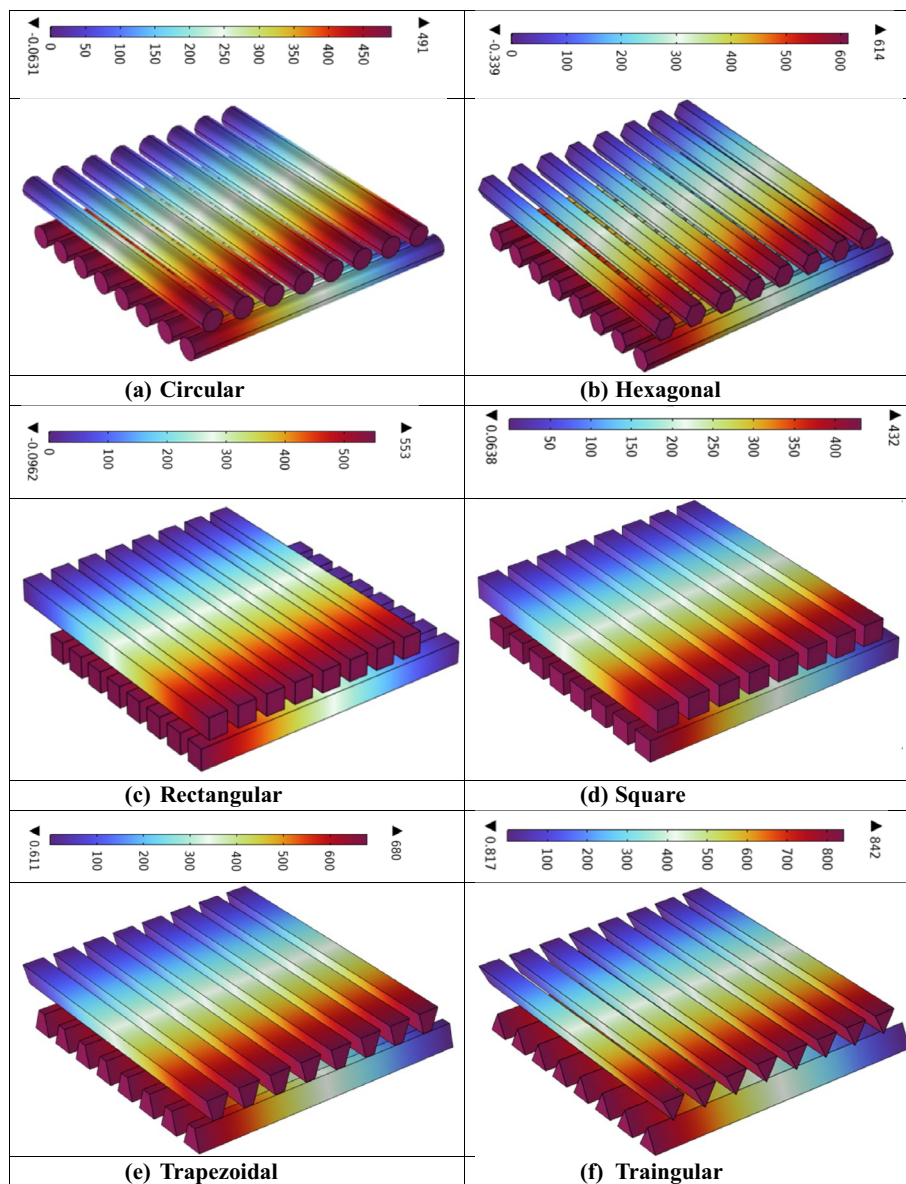

Fig. 7 Surface pressure for different shaped CFMCHE at *Re* = 8 and channel distance 35 μm

Figure 6 displays the isothermal contours over six different-shaped microchannels, with 8 channels, 35 μm channel distance, and $Re = 20$. We observe from Fig. 6 that in cold channels, the fluid temperature color is getting more yellow, which is getting hotter, and the hot channel's outlet temperature in the context of trapezoidal forms is 314.26*K*, which is higher than other shapes; in the case of triangular shapes, it is 313.90*K*, which is less than trapezoidal shapes. Most isothermal lines in a trapezoidal channel are yellow after half the channel length and at the cold outlet, which denotes a higher heat transmission. A cold channel has an outlet temperature of 315.20 K, more significant than other geometries' outlet temperatures. Aside from this, the temperature in the triangular channel is 314.26 K, the lowest temperature in the circular channel is 313.03 K, and the remaining channels have temperatures ranging from 313 to 314 K.
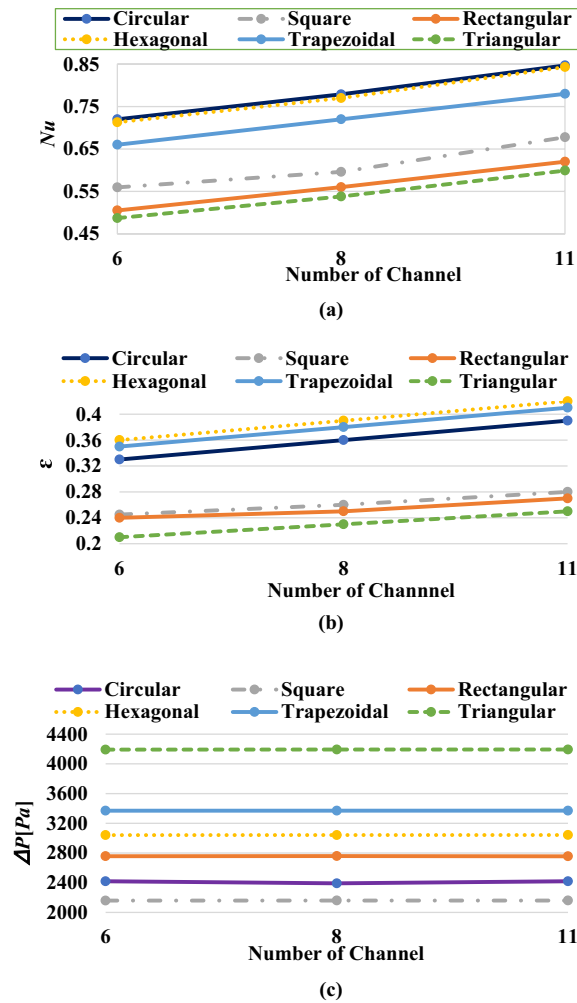

Fig. 8 **a** Nusselt number (**b**) effectiveness (**c**) pressure drops with the channel number of CFMCHE
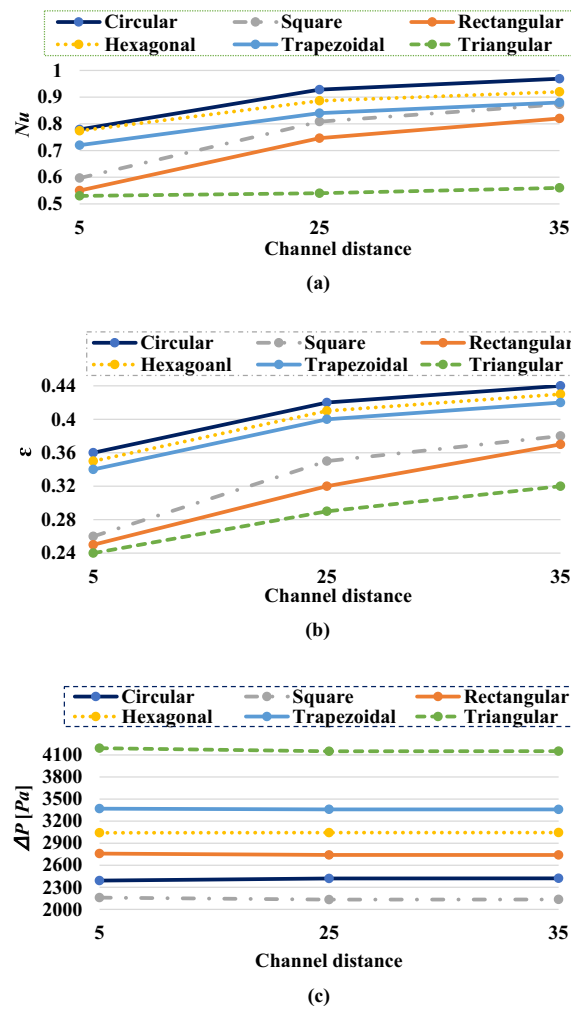
Fig. 9 **a** Nusselt number, (**b**) effectiveness, and (**c**) pressure drop for channel distance variation

Surface pressure

Figure 7 illustrates how different microchannel forms affect pressure drop, where *Re* and channel number are fixed at 8 and channel distance at 35 μm. A color legend with maximum and minimum values is included in this figure. According to Fig. 7, the pressure drop varies between 0.817 Pa and 842 Pa, with triangle shapes experiencing the maximum pressure drop and square shapes experiencing the lowest pressure drop, which ranges between 0.064 Pa and 432 Pa. In that order, the pressure drops are 680 Pa, 553 Pa, 491 Pa, and 614 Pa, in the remaining trapezoidal, rectangular, circular, and hexagonal shapes. Therefore, triangle shapes have the most significant pressure decreases, and square shapes have the lowest.

Role of channel number

Figures 8a–c illustrate how the number of channels affects the *Nu* number, effectiveness, and pressure drops, respectively. The channel distance stays constant at 5 and Reynold numbers stay constant at 20 for all channel shapes (circular, square, hexagonal, trapezoidal, triangular, and rectangular), but channel numbers 6, 8, and 11 vary. Nusselt

number, efficiency, and pressure drop are calculated accordingly using Eqs. (10), (14), and (11), respectively. Figure 8a shows that a rectangular channel has the lowest Nusselt number, 0.60, and a circular channel has the highest, 0.85, at channel 11. It is observed that Nu is the highest for circular shapes, but its increasing rate is highest for square shapes (21.13%), while the rate for channels with a circular shape is 17.64%. Figure 8b shows that a hexagonal channel produces the maximum efficiency value (0.42), while a triangular channel produces the lowest (0.25) at Reynold number 20. As we can see, the effectiveness growth rate for the circular channel is 18.18%; however, the effectiveness growth rate for the hexagonal channel is 16.67%, as shown by the yellow shade in this graph. As seen in Fig. 8c, the conduit with a triangular shape has the most significant pressure drop, 4192.9 Pa; the square-shaped duct, on the other hand, has the lowest pressure decrease 2159.8 Pa, at channel number 6. Furthermore, we observe that the pressure decrease is unaffected by raising the channel number.

Role of channel distance

The channel distance varies between 5 μm, 25 μm, and 35 μm when the channel number is fixed at 8, and the Reynolds number at 20, and the heat exchanger's size and shape remain constant for all of the following channel shapes: circular, square, hexagonal, trapezoidal, triangular, and rectangular. Figure 9a–c show the variation of the Nu number, effectiveness, and the pressure decrease via the channel distance fluctuation, respectively. The findings exhibit that the Nu value for the triangular-shaped channel is the lowest at 0.56, while the most outstanding value is 0.96 for a circular channel. The graph shows that, despite having the highest heat transfer rate, circular channels only have an increasing rate of 24.41%, which is 24.68% less than that of rectangular channels, which have the highest growth rate of 49.09%, and the lowest increase rate of 5.66% for triangular channels.

Graph 9b shows that a triangular channel yields the lowest efficiency, 0.32, which is opposite to that value when we change the channel number. Besides, a circular channel has the highest value, 0.44 at a distance of 35 μm. We can observe that the effectiveness growth rate for square-shaped channels is around 46.15%, the highest rate in this area, and 10.26% for hexagonal, which is the lowest. On the other hand, this graph indicates that the effectiveness growth rate for trapezoidal-shaped channels is just 17.95%. Figure 9c shows that the decrease rate is small, as it only amounts to 0.10% for a hexagonal channel.

Role of Reynolds number

Figure 10a, c demonstrate the impact of Re number variations on pressure drop and Nu number across six different shapes for laminar flow with a fixed channel distance of 35 μm and a fixed number of eight, respectively. Figure 10b depicts the error bar graph of the demonstrated number. The inlet velocities for $Re = 2, 6, 8, 10, 12, 14, 16, 18,$ and 20 are 0.024 ms^{-1}, 0.05 ms^{-1}, 0.07 ms^{-1}, 0.09 ms^{-1}, 0.122 ms^{-1}, 0.14 ms^{-1}, 0.17 ms^{-1}, 0.19 ms^{-1}, 0.22 ms^{-1}, and 0.24 ms^{-1} for the square-shaped channel. The rise in Reynolds number and the Nu number are always seen simultaneously as Fig. 10a illustrates. From this figure, we notice that the Nusslet number for circular-shaped channels is the highest
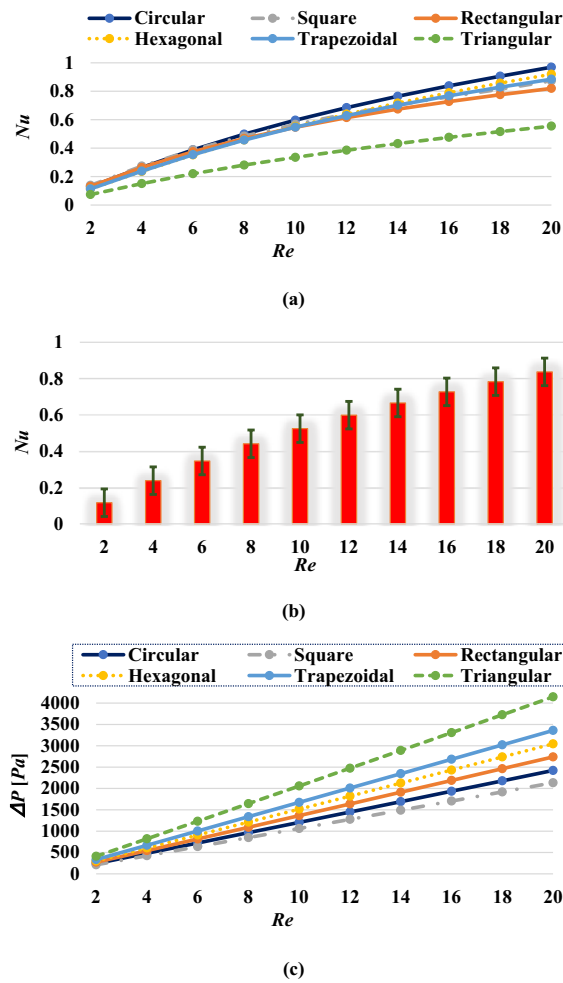
Fig. 10 **a** *Nu* values, **b** error bar, and **c** pressure drop for *Re* fluctuation

when $Re = 20$; it is 0.96 for circular shapes and 0.82, 0.87, 0.92, 0.88, and 0.55 for hexagonal, rectangular, square, trapezoidal, and triangular shapes, respectively; however, the rate at which the Nusslet number rises for trapezoidal shapes is 16.46%, which is 0.78% higher than the circular one when *Re* is set at 20.

The error bar graph in Fig. 10b shows the heat transfer rate error for various Reynolds values between 2 and 20. We have determined the average and standard deviation using values of the Nusselt numbers. Each red bar has a tiny green line at the top representing the error margin, a measure of variability or uncertainty. All of the *Re* values have relatively small error bars, which suggests that the *Nu* measurements and computations are accurate and consistent. When *Re* increases, the errors rise somewhat but stay within a reasonable range in the observed or estimated *Nu* values. Utilizing the data supplied by *Nu*, we create an error bar with a maximum average value of 0.84, a minimum average value of 0.11, and a maximum standard deviation of 0.15 and a minimum standard deviation of 0.02. The tiny error bars indicate the well-controlled experimental or simulation setup and the consistent *Nu* values. We may conclude that the findings in this study are precisely correct in terms of being short-tailed based on the length of the tail.
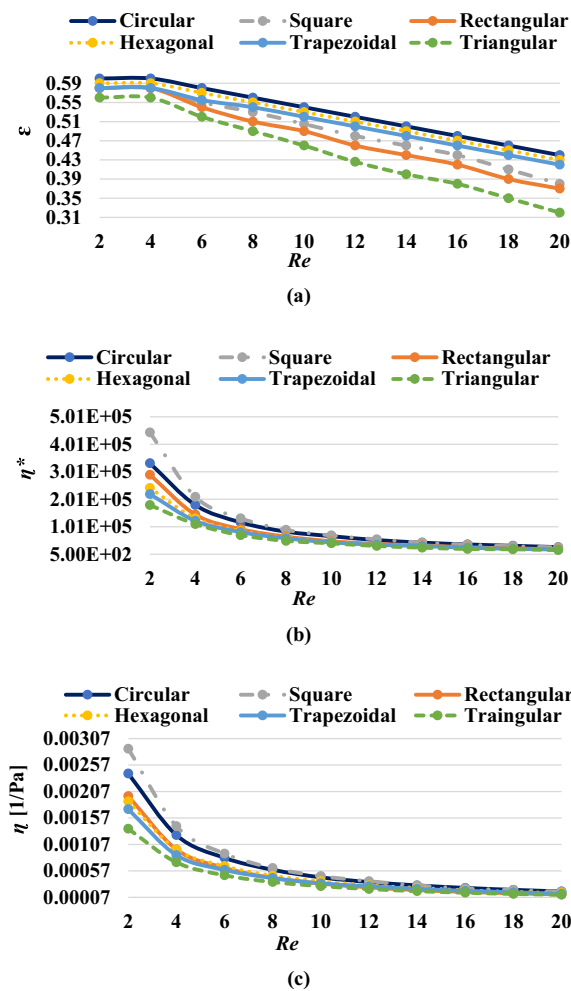
Fig. 11 **a** Effectiveness, **b** Hydraulic performance index (η^*), and **c** Thermal performance index (η) for different Re

Figure 10c shows us that, of all these shapes, triangles have the highest pressure drop, at 4145.207 Pa, while the pressure drops of the other shapes are all under 3000 Pa, and the lower pressure drop is 2134.34 Pa at $Re = 20$ for square shapes. This is because triangles have a small cross-sectional area. The increasing rate of pressure decrease in the case of a square shape is 51.23% smaller than that of a triangular shape, which is considered to be the lowest one for being high and has a maximum cross-sectional area compared to others, even though CFMCHE's basic geometry is the same in each instance.

The variation of effectiveness, hydraulic and thermal performance index for changing Reynolds number ranges between 2 and 20, shown in Fig. 11a–c, respectively, through six different-shaped CFMCHEs with a constant Channel distance of 35 μm. Effectiveness increases constantly for square, rectangular, hexagonal, and circular shapes before declining in the case of $Re < 4$, increasing overall due to higher flow velocities; triangular and trapezoidal channels show a progressive decline in effectiveness. As per the computation, the efficiency of a triangular-shaped heat exchanger is reduced by high

fluid velocity (0.39 ms^{-1}), resulting in an effectiveness of 0.55. Similarly, the efficacy of a circular-shaped CFMCHE is higher (0.60) as the fluid velocity is 0.24 ms^{-1}.

A performance index's definition and the things it measures determine whether it is dimensional or dimensionless. Many performance indices are designed to be dimensionless, meaning they don't have physical units. They are often ratios of two quantities with the same units, canceling out the units. For example, if a performance index combines heat transfer rates and pumping power, it is typically dimensionless, as it's the ratio of physical quantities with the same units. However, there are cases where a performance index might have dimensions, especially if it combines multiple physical quantities with different units. For instance, a performance index combining effectiveness and pressure drop could have dimensions, representing a trade-off between two quantities with different units.

When evaluating the performance of a microchannel heat exchanger, two important ratios often considered are the ratio of heat transfer rate to pumping power and the ratio of heat transfer rate to pressure drop or efficiency to pressure drop. These ratios help differentiate between thermal performance and hydraulic performance. Both indices are crucial for evaluating the overall performance of a heat exchanger. Optimizing these ratios ensures that the heat exchanger operates thermally and hydraulically efficiently. Thermal performance index is the ratio of efficiency to pressure drop or the ratio of heat transfer rate over pressure drop which is dimensional. Hydraulic performance index is the ratio of heat transfer rate to pumping power which is dimensionless.
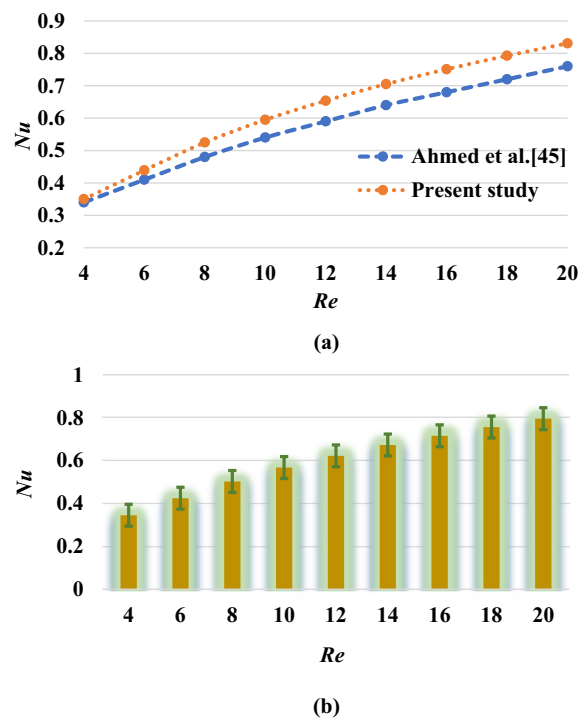

Fig. 12 a Comparison and (**b**) error bar of *Nu* number against *Re* between Ahmed et al. [45] and the present numerical study

Because square channels have the lowest pressure drop and triangle channels have the most detrimental pressure drop of all other shaped channels, it is evident from Fig. 11b, c that square channels have the highest and triangular channels have the lowest hydraulic performance and thermal performance. In this instance, the only explanation is that when the Reynolds number increases, more pressure falls and a decrease in effectiveness. The reduction in heat transfer rate with increasing pumping power is directly correlated with the *Re* number; additionally, the triangular channel experiences the highest rate of decline (94.34%), while the hexagonal-shaped channel experiences the lowest rate (92.50%) is 5.22% higher than all other shapes at $Re = 2$. It is evident from diagram 11c that channels with a square form have a better performance index (53.57%) than channels with triangular shape at Reynolds number 2.

Comparison

Due to Nusselt number

With water being the base fluid, the comparison between the current study and Ahmed et al. [45] is displayed in Fig. 12a for the variation of *Nu* as a function of *Re*. They [45] investigated two distinct scenarios: water and water-Al_2O_3 pair nanofluid, and they carried out CFD analysis of flow and heat transfer enhancement using water-alumina nanofluid through a CFMCHE composed of stainless steel. The size of their microchannel is 800×800 μm. They have used five distinct rectangular-shaped channels. We maintain all conditions and properties and compare our channel data in rectangular shape with their first case of numerical data. The GetData Graph Digitizer program extracts the data for this comparison from [45]. The results of this study and Ahmed et al. [45] fit each other quite well.

Figure 12b shows the relationship between the Reynolds number (*Re*) and the Nusselt number (*Nu*) using an error bar graph. The Nusselt number measurement uncertainty
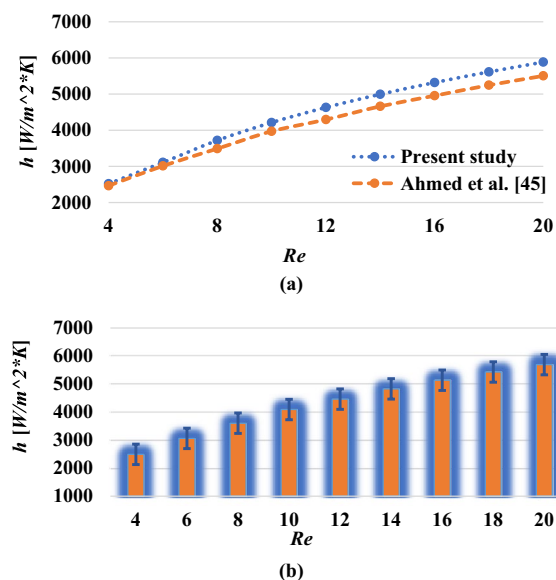

Fig. 13 **a** Comparison and (**b**) error bar of *versus Re* between Ahmed et al. [45] and the present data

is shown by the vertical lines with caps on each bar, and a clear rising trend in the Nusselt number is observed as the Reynolds number increases This implies that convective exchange of heat improves with increasing flow rate (and hence Reynolds number), which is characteristic behavior in heat transfer systems. Relatively short error bars for lower Reynolds numbers ($Re = 4$ and 6) suggest more consistent measurements. Even at higher flow rates, the measurements are accurate as evidenced by the short error bars that remain as Re increases, particularly at $Re = 20$. We have calculated the error graph by calculating the mean and standard deviation values: 0.79–0.35 and 0.05–0.01, respectively. The reasonable proximity of the mean and standard deviation values leads us to the conclusion that the data are appropriate.

Due to heat transfer coefficient

We evaluate our results with the fluctuation of the heat transfer coefficient (h) against Re, provided by Ahmed et al. [45]. Figures 13a, b display the comparative results and error bar plot between Ahmed et al.'s study and the current one. Figure 13b shows the relationship between the Reynolds number (Re) and the heat transfer coefficient (h) using an error bar graph. The heat transfer coefficient is roughly 2000 $W/(m^2K)$ at the lowest Reynolds number and rises to 20 before reaching roughly 6000 $W/(m^2K)$. This threefold rise demonstrates the flow rate's major influence on the microchannel heat exchanger's heat transfer efficiency. For lower Reynolds numbers ($Re = 4$ and 6), relatively short error bars indicate more consistent measurements. The error graph is created by computing the mean and standard deviation, which are 5610.99–2409.487 and 152.11–77.84, respectively. The reasonable proximity of the mean and standard deviation values leads us to conclude that the data are appropriate and we find a good agreement with Ahmed et al. [45].

Regression and residual

Regression equation

The above results and discussions show that square-shaped CFMCHE gives a higher effectiveness and performance index than other shapes. The results of this research lead to the development of a new multiple variable linear regression equation of performance index (η), in terms of inertia force, i.e., Reynolds number ($Re = 2$–20), channel number ($N_{ch} = 4$–11), and channel distance ($D_{ch} = 5$–35 μm) for the square shaped CFMCHE such as:

$$\eta = 0.003151 - 0.0002Re + 3.69 10^{-5}N_{ch} + 1.04 10^{-5}D_{ch},$$

With a total degree of freedom of 100 (regression 3, residual 96). The multiple R (correlation coefficient) is 0.8026, the adjusted R-squared is 0.6331, the R-square (R^2) value is 0.6442, the standard error is 0.0009, and the significance F (p-value) associated with this equation is 1.82571×10^{-21}. This regression equation is statistically and enormously significant.
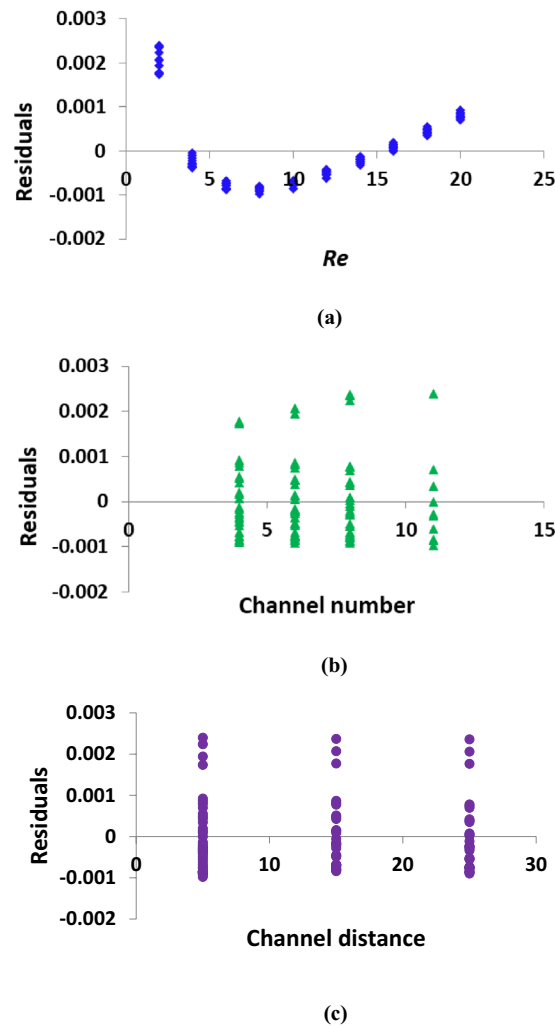
Fig. 14 Residual error plots of performance index for (**a**) *Re*, (**b**) N_{ch}, and (**c**) D_{ch}

Residual plots

A residual error plot is a graphical representation of the differences between predicted values and actual measured values in a model, playing a vital role in assessing the performance of heat and mass transfer models and helping researchers and engineers make informed decisions about model accuracy and potential areas for improvement. Figure 14a–c represents the residual errors of the performance index of the square-shaped CFMCHE regarding the *Re* number, channel number, and channel distance, respectively. These figures are validated using parametric residual plots, highlighting the model's accuracy and dependability by continually showing minimal residual.

Conclusions

Fluid flow and heat transfer characteristics through six distinct shapes of CFMCHE are studied computationally in the present work using water as a base fluid by observing three cases: the impact of fluctuating channel distance, the influence of changing

channel number, and the influence of changing Re number. Drawing from these findings, the subsequent deduction can be made:

- The pressure drop varies slightly as the channel number changes, but the values of Nu and efficiency rise as the channel number does. Even though Nu is the maximum for circular-shaped, Nu has a higher increasing rate for square-shaped (21.13%) than circular-shaped (17.64%).
- Circular channels show the highest effectiveness increase rate at 18.18% and a pressure drop rate at 0.44%, indicating a 77.27% higher rate than square channels. Square channels show an effectiveness increase rate of 14.29% and a pressure drop increase rate of 0.10%.
- Together, Re and Nu's impacts intensify. In contrast to hexagonal shapes, circular and trapezoidal shapes have a rising rate of about 16%, which is 1.1% higher than others. However, all shapes have a more significant pressure drop than square ones, with the trapezoidal shape declining 90.07%.
- Re number determines the rate at which heat transfer decreases over pumping power; additionally, the rate of decline is lowest for trapezoidal channels (91.91%).
- The effectiveness decreasing rate is highest for triangular shapes (42.86%) and lowest for hexagonal shapes (26.67%), where the effectiveness decreasing rate for square shapes is 36.67%, which is acceptable compared to circular and triangular in the case of Re number.
- The Nu, pressure drop, and efficacy all change as we adjust the channel distance. The Nusselt number increasing rate is 46.28% for square-shaped channels, and for rectangular shapes is 49.09%, the highest compared to all the shapes.
- The effectiveness growth rate for square-shaped channels is around 46.15%, the highest rate, and 10.26% for hexagonal which is the lowest rate when we adjust channel distance.
- The Δp decreasing rate is 1.16% for square-shaped channels, and besides, this Δp decreasing rate is also negligible for all other shapes like square ones when we change channel distance.
- The performance index of all-shaped microchannel heat exchangers with constant Channel distance decreases as Re increases. The best-performing channels (53.57%) among all shapes undoubtedly have a square for Reynold's number 2, channel number 8, and channel distance 35.
- The optimal Nu is obtained at Reynolds number 20, channel distance 35 μm, and channel number 8 for square-shaped CFMCHE in our experiment where cap N u equals 0.87 is the highest of all other combinations for square-shaped channels.

We demonstrate that our mesh element is too huge, just like in the grid test. Because of this and the convergence requirements, it is occasionally challenging to compute continuously. In addition, because our university needs more laboratory aid, using parametric sweep makes it difficult to run this application because it requires a more powerful computer configuration. We could also achieve more significant results if we combined numerical and experimental work, but we need a laboratory facility.

List of symbols

A	Cross-sectional area of CFMCHE (m^2)
C_p	Specific heat ($Jkg^{-1}K^{-1}$)
D_h	Hydraulic diameter (m)
D_{ch}	Distance between channels (μm)
H	Computational domain height (μm)
L	Length of the computational domain μm)
m	Mass flow rate ($kg.s^{-1}$)
N_{ch}	Number of channels
P	Pressure (Pa)
P_{pu}	Pumping Power (W)
ΔP	Total pressure drop (Pa)
Re	Reynolds Number
T	Temperature (K)
Nu	Nusselt number
W	Computational domain width (μm)
W_{ch}	Width of channel (μm)
Q	Volumetric flow rate ($m^3 s^{-1}$)
q	Heat transfer (W)
u, v, w	Co-ordinates velocity (ms^{-1})

Greek symbols

η	Thermal performance index (Pa^{-1})], $\eta = \frac{\varepsilon}{\Delta P}$
η^*	Hydraulic performance index, $\eta^* = \frac{q}{P_{pu}}$
ε	Heat exchanger effectiveness
μ	Dynamic viscosity (Nsm^{-2})
κ	Thermal conductivity ($Wm^{-1}K^{-1}$)
ρ	Density kgm^{-3})

Subscripts

c	Cold
ch	Channel
f	Base fluid
h	Hot
i	Inlet
in	Inflow
or	Origin
out	Outlet
s	Solid
w	Water
max	Maximum
min	Minimum

Author contributions
The first author does the job. The second author edits, modifies, supervises the research, and completes necessary corrections.

Availability of data and materials
No data and material are available.

Declarations

Competing interests
There is no competing interest.

References

1. Khairul MA, Alim MA, Mahbubul IM, Saidur R, Hepbasli A, Hossain A. Heat transfer performance and exergy analyses of a corrugated plate heat exchanger using metal oxide nanofluids. Int Commun Heat Mass Transfer. 2014;50:8–14. https://doi.org/10.1016/j.icheatmasstransfer.2013.11.006.
2. Yaïci W, Ghorab M, Entchev E. 3D CFD analysis of the effect of inlet air flow maldistribution on the fluid flow and heat transfer performances of plate-fin-and-tube laminar heat exchangers. Int J Heat Mass Transf. 2014;74:490–500. https://doi.org/10.1016/j.ijheatmasstransfer.2014.03.034.
3. Ajeeb W, da Silva RRST, Murshed SMS. Experimental investigation of heat transfer performance of Al_2O_3 nanofluids in a compact plate heat exchanger. Appl Therm Eng. 2023;218(1–11):119321. https://doi.org/10.1016/j.applthermaleng.2022.119321.
4. Cao Y, Salem Md, Elmasry Y, Galal AM, Singh PK, Gepreel KA, Nguyen VG, Buswig YM, Nguyen PQP, Wae-hayes M. Flow and heat transfer in a plain fin-and-hexagonal tube heat exchanger with different side ratios. Case Stud Therm Eng. 2022;38(1–13):102376. https://doi.org/10.1016/j.csite.2022.102376.
5. Natesan K, Karinka S. A comprehensive review of heat transfer enhancement of heat exchanger, heat pipe and electronic components using graphene. Case Stud Therm Eng. 2023;45(1–16):102874. https://doi.org/10.1016/j.csite.2023.102874.
6. Ismail LS, Ranganayakulu C, Shah RK. Numerical study of flow patterns of compact plate-fin heat exchangers and generation of design data for offset and wavy fins. Int J Heat Mass Transf. 2009;52:3972–83. https://doi.org/10.1016/j.ijheatmasstransfer.2009.03.026.
7. Ghasemi A, Elham A. Multi-objective topology optimization of pin-fin heat exchangers using spectral and finite-element methods. Struct Multidiscip Optim. 2021;64:2075–95.
8. Kalantari H, Ghoreishi-Madiseh SA, Kurnia JC, Sasmito AP. An analytical correlation for conjugate heat transfer in fin and tube heat exchangers. Int J Therm Sci. 2021;164:1–17. https://doi.org/10.1016/j.ijthermalsci.2021.106915.
9. Raei B, Peyghambarzadeh SM, Asl RS. Experimental investigation on heat transfer and flow resistance of drag-reducing alumina nanofluid in a fin-and-tube heat exchanger. Appl Therm Eng. 2018;144:926–36. https://doi.org/10.1016/j.applthermaleng.2018.09.006.
10. Lima CCXS, Ochoa AAV, da Costa JAP, de Menezes FD, Alves JVP, Ferreira JMGA, Azevedo CCA, Michima PSA, Leite GNP. Experimental and computational fluid dynamic—CFD analysis simulation of heat transfer using graphene nanoplatelets GNP/water in the double tube heat exchanger. Processes. 2023;11:2735. https://doi.org/10.3390/pr11092735.
11. Khosravi A, Campos H, Malekan M, Nunes RO, Assad MEH, Machado L, GarciaPabon JJ. Performance improvement of a double pipe heat exchanger proposed in a small-scale CAES system: an innovative design. Appl Therm Eng. 2019;162:114315. https://doi.org/10.1016/j.applthermaleng.2019.114315.
12. Shirvan K, Mamourian M, Mirzakhanlari S, Ellahi R. Numerical investigation of heat exchanger effectiveness in a double pipe heat exchanger filled with nanofluid: a sensitivity analysis by response surface methodology. Powder Technol. 2017;313:99–111. https://doi.org/10.1016/j.powtec.2017.02.065.
13. Bashtani I, Esfahani JA. ε-NTU analysis of turbulent flow in a corrugated double pipe heat exchanger: a numerical investigation. Appl Therm Eng. 2019;159: 113886.
14. Nasrin R, Sweety SA, Zahan I. Turbulent nanofluid flow analysis passing a shell and tube thermal exchanger with Kays-Crawford model. J Nanofluids. 2021;10:518–37. https://doi.org/10.1166/jon.2021.1803.
15. Gunnasegaran P, Mohammed HA, Shuaib NH, Saidur R. The effect of geometrical parameters on heat transfer characteristics of the microchannels heat sink with different shapes. Int Commun Heat Mass Transf. 2010;37:1078–86. https://doi.org/10.1016/j.icheatmasstransfer.2010.06.014.
16. Zhu Q, Su R, Xia H, Zeng J, Chen J. Numerical simulation study of thermal and hydraulic characteristics of laminar flow in a microchannel heat sink with water droplet cavities and different rib columns. Int J Therm Sci. 2022;172(107319):1–15. https://doi.org/10.1016/j.ijthermalsci.2021.107319.
17. Mellas IE, Samkhaniani N, Falsetti C, Stroh A, Icardi M, Magnini M. Numerical investigation of bubble dynamics and flow boiling heat transfer in cylindrical micro-pin-fin heat exchangers. Int J Heat Mass Transf. 2024;228(125620):1–19. https://doi.org/10.1016/j.ijheatmasstransfer.2024.125620.
18. Mohammed HA, Bhaskaran G, Shuaib NH, Abu-Mulaweh HI. Influence of nanofluids on parallel flow square microchannel heat exchanger performance. Int Commun Heat Mass Transfer. 2011;38(1):1–9. https://doi.org/10.1016/j.icheatmasstransfer.2010.09.007.
19. Al-Nimr MA, Muqableh M, Khadrawi AF, Ammourah SA. Fully developed thermal behaviors for parallel flow microchannel heat exchanger. Int Commun Heat Mass Transf. 2009;36:385–90. https://doi.org/10.1016/j.icheatmasstransfer.2009.01.010.
20. Kragh J, Rose J, Nielsen TR, Svendsen S. New counter flow heat exchanger designed for ventilation systems in cold climates. Energy Build. 2007;39:1151–8. https://doi.org/10.1016/j.enbuild.2006.12.008.
21. Anjaneya G, Sunil S, Kakkeri S, Math MM, Vaibhav MN, Solaimuthu C, Prasad CD, Vasudev H. Numerical simulation of microchannel heat exchanger using CFD. Int J Interact Design Manuf (IJIDeM). 2023. https://doi.org/10.1007/s12008-023-01376-8.
22. Kalantari D, Tafakhori M, Ghanbari M, Biparva P, Peyghambarzadeh SM. Intensification of thermal efficiency of a cross-flow heat exchanger under turbulent flow conditions using $CuFe_2O_4$/water nanofluid, International Journal of Thermal Sciences. Int J Therm Sci. 2023;185(1–15):108107.
23. Masitah ARS, Ahmad MI, Yatim YM. Heat transfer and effectiveness analysis of a cross-flow heat exchanger for potential energy recovery applications in hot-humid climate. Energy Res J. 2015;6(1):1–11.
24. Li W, Jin M, Liu C, Li W, Song Y, Zhou T, Jiang J, Bai Y. Numerical investigation of thermal-hydraulics characteristics of cross-flow corrugated plate heat exchanger for lithium-cooled space nuclear reactor. Appl Therm Eng. 2024;238(1–16):121931.
25. Furlong AJ, Ge H, Hughes RW, Macchi A, Haelssig JB. Dynamic modelling of cross-flow printed circuit heat exchangers for multistage reactor intercooling. Appl Therm Eng. 2024;239(1–14):122010. https://doi.org/10.1016/j.applthermaleng.2023.122010.

26. Nogueira É. Theoretical thermal performance of cross-flow finned heat pipe heat exchanger used for air conditioning in surgery rooms. Mech Eng Adv. 2023;1(1):131. https://doi.org/10.59400/mea.v1i1.131.
27. Ghorbani M, Wang H. Computational modeling and experiment validation of a microchannel cross-flow heat exchanger. Int Commun Heat Mass Transfer. 2023;149(107116):1–15. https://doi.org/10.1016/j.icheatmasstransfer.2023.107116.
28. Liu Y, Li K, Wen J, Wang S. Thermodynamic characteristics of counter flow and cross flow plate-fin heat exchanger based on distributed parameter model. Appl Therm Eng. 2023;219(119542):1–17. https://doi.org/10.1016/j.applthermaleng.2022.119542.
29. Mangrulkara CK, Dhoblea AS, Chamolib S, Guptab A, Gawande VB. Recent advancement in heat transfer and fluid flow characteristics in cross flow heat exchangers. Renew Sustain Energy Rev. 2019;113:109220. https://doi.org/10.1016/j.rser.2019.06.027.
30. Moosavi A, Ljung A, Lundström TS. A comparative study on thermo-fluid characteristics of free and wall-bounded cross-flow heat exchangers. Therm Sci Eng Progr. 2023;40(101746):1–18. https://doi.org/10.1016/j.tsep.2023.101746.
31. Jradi R, Marvillet C, Jeday MR. Parametric study of calcium sulfate crystallization fouling in cross-flow heat exchanger using response surface methodology. Heat Mass Transfer. 2023;59:1971–85. https://doi.org/10.1007/s00231-023-03368-6.
32. Toolthaison S, Kasayapanand N. Heat transfer enhancement in a cross-flow heat exchanger with modified air angles of attack. J Energy Eng. 2016;142:04015044. https://doi.org/10.1061/(ASCE)EY.1943-7897.0000316.
33. Caceres C, Ortega A, Jones GF. Dynamic modeling of a refrigerant-based cross-flow heat exchanger for close-coupled hybrid cooled data centers. In: 2023 22nd IEEE Intersociety Conference on Thermal and Thermomechanical Phenomena in Electronic Systems (ITherm), Orlando, FL, USA, 2023, pp. 1–9, https://doi.org/10.1109/ITherm55368.2023.10177550.
34. Starace G, Fiorentino M, Longo MP, Carluccio E. A hybrid method for the cross flow compact heat exchangers design. Appl Therm Eng. 2017;111:1129–42. https://doi.org/10.1016/j.applthermaleng.2016.10.018.
35. Alonso MJ, Liu P, Mathisen HM, Ge G, Simonson C. Review of heat/energy recovery exchangers for use in ZEBs in cold climate countries. Build Environ. 2015;84:228–37. https://doi.org/10.1016/j.buildenv.2014.11.014.
36. Mortean MVV, Cisterna LHR, Paiva KV, Mantelli MBH. Thermal and hydrodynamic analysis of a cross-flow compact heat exchanger. Appl Therm Eng. 2019;150:750–61. https://doi.org/10.1016/j.applthermaleng.2019.01.038.
37. Mitra I, Ghosh I. Axial conduction in cross-flow heat exchangers: an analytical approach to the coupled heat transfer problem. Int J Heat Mass Transf. 2023;200:123502. https://doi.org/10.1016/j.ijheatmasstransfer.2022.123502.
38. Zhong Q, Yang L, Tao Y, Luo C, Xu Z, Xi T. An optimized crossflow plate-fin membrane-based total heat exchanger. Energy Build. 2015;86:550–6. https://doi.org/10.1016/j.enbuild.2014.10.036.
39. Kang SW, Tseng SC. Analysis of effectiveness and pressure drop in micro cross-flow heat exchanger. Appl Therm Eng. 2007;27:877–85. https://doi.org/10.1016/j.applthermaleng.2006.09.002.
40. Ghachem K, Aich W, Kolsi L. Computational analysis of hybrid nanofluid enhanced heat transfer in cross flow micro heat exchanger with rectangular wavy channels. Case Stud Therm Eng. 2021;24(100822):1–14. https://doi.org/10.1016/j.csite.2020.100822.
41. Al-Baghdadi MARS, Noor ZMH, Zeiny A, Burns A, Wen D. CFD analysis of a nanofluid-based microchannel heat sink. Therm Sci Eng Progr. 2020;20:100685.
42. Hasan MI, Rageb AA, Yaghoubi M, Homayoni H. Influence of channel geometry on the performance of a counter flow microchannel heat exchanger. Int J Therm Sci. 2009;48:1607–18.
43. Zienkiewicz OC, Taylor RL. The finite element method. McGrow-Hill. 1989;2:16–48.
44. Zahan I, Nasrin R, Jahan S. Ionanofluid flow through a triangular grooved microchannel heat sink: thermal heightening. Heliyon. 2023;9(8):e18938. https://doi.org/10.1016/j.heliyon.2023.e18938.
45. Ahmed SS, Ghyadh NA, Al-Baghdadi MARS. CFD investigation of flow and heat transfer enhancement in cross flow microchannel heat exchanger using nanofluid. J Mech Eng Res Dev. 2021;44(5):358–70.
46. Priam SS, Nasrin R. Oriented magneto-conjugate heat transfer and entropy generation in an inclined domain having wavy partition. Int Commun Heat Mass Transfer. 2021;126: 105430. https://doi.org/10.1016/j.icheatmasstransfer.2021.105430.
47. Xia GD, Jiang J, Wang J, Zhai YL, Ma DD. Effects of different geometric structures on fluid flow and heat transfer performance in microchannel heat sinks. Int J Heat Mass Transf. 2015;80(439–447):10. https://doi.org/10.1016/j.ijheatmasstransfer.2014.08.095.

Publisher's Note